Valentin Zuchuat[1-2] – IAS Postdoctoral Grant Report 2023 Session 1

New insights (and new questions) on the depositional environment and dynamics of the lowermost Triassic in Svalbard using sedimentology, radiochronology, palaeontology, and provenance data

In collaboration with: Julian Janocha[3-4-5], Beverly S. Felten[2], Hannah L. Brooks[2], Stella Z. Buchwald[6], Brian Beaty[7], Lidya Tarhan[7], Lard Eivind Augland[8], and William J. Foster[6]

[1]CSIRO Mineral Resources, Australia; [2]Geological Institute, RWTH Aachen, Germany; [3]Department of Geosciences, UiT – The Arctic University of Norway, Norway; [4]Department of Arctic Geology, University Centre in Svalbard, Norway; [5]Equinor ASA, Norway; [6]Department of Earth System Sciences, Universität Hamburg, Germany; [7]Department of Earth and Planetary Sciences, Yale University, New Haven CT, USA; [8]Department of Geosciences, University of Oslo, Norway

1. Introduction and rationale

The Permian-Triassic transition is closely related to one of the most dramatic mass extinctions that the Earth has experienced: the End-Permian Mass Extinction (EPME), which occurred ca. 252 Ma (Burgess et al., 2014). Overall, palaeoenvironmental changes occurring at that time are well constrained, as they heavily impacted the bio-, hydro-, and atmosphere, as recorded by a range of proxy records. However, although these environmental changes are well documented, and several have been tied to the contemporaneous eruption and emplacement of the Siberian Traps Large Igneous Province (LIP, Svensen et al., 2009), how volcanism drove downstream environmental changes and how the latter in turn interacted to mediate cascading ecological collapse, heighten extinction risk and delay ecosystem recovery remain disputed (Smyrak-Sikora et al., in review, and references therein).

The remote regions of Canada, Greenland, and Svalbard in the High Arctic provide a window into the northern margin of Pangaea during the Permian and Triassic periods (Fig. 1). In Svalbard, the Permian–Triassic transition occurs between the weathering-resistant, spiculitic mudstones of the Kapp Starostin Formation (Cutbill and Challinor, 1965) and soft, weatherable siliciclastic-dominated Vardebukta and Vikinghøgda formations (Fig. 1-2; Mørk et al., 1982, 1999a). Throughout the years, geologists in Svalbard have meticulously studied these sedimentary successions, with a specific geochemical focus on the boundary interval itself and lowermost Triassic strata—the interval deposited shortly before, during, and after the EPME, and which records a major supra-regional transgression occurring very rapidly at the very end of the Permian (Mørk et al., 1989). Overlying Triassic strata have been the target of extensive sedimentology and basin analysis studies and served as an analogue for the subsurface deposits of the Barents Shelf (Dallmann, 1999). However, the physiography of the basin at the time was a little bit more complex, with areas experiencing near-continuous sedimentation from the Carboniferous to the Early Triassic (i.e. Festningen and Reinodden sections; Fig. 1-2), contrasting with structural highs subaerially exposed since the Visean (Mississippian), such as the Sørkapp-Hornsund High (SHH) in southern Spitsbergen (Fig. 1-3-4; Dallmann, 1999). There, Carboniferous continental rocks are directly overlain by an up-to-10 cm thick tephra layer, Lower Triassic near-coastal conglomerates of unknown provenance (Brevassfjellet Beds in Mørk et al., 1999b), fossiliferous limestone, and shallow-marine to shelfal siliciclastic sediments, all of which belong to the Vardebukta Formation. Fossils collected from these shallow-marine, fossiliferous limestone beds overlying the conglomerates (Fig. 3-4) suggest marine sedimentation started during the Dienerian Age at the latest (late Induan Stage, Early Triassic; Zuchuat, 2014). Yet, and in contradiction to local fossil records, most major publications on the Triassic of the Barents Sea indicate an onset of

sedimentation over the SHH (and Greenland) more than 10 Ma later during the Ladinian Stage (late Middle Triassic; e.g. Fig. 3 in Gilmullina et al., 2021). In addition to uncertainty with regards to the age of these conglomeratic deposits, their provenance remains totally unknown, and the overall sedimentation and flooding history of the SHH differs from areas north of the High.

Questions therefore remain as to how and why the Svalbard basin changed during the Late Permian and the Early Triassic. This especially regards the continental-to-marine transect extending from the SHH areas, which had been subaerially exposed for ca. 75 Myr, to more shelfal systems north of the SHH which experienced continuous deposition throughout most of the Permian and the Early Triassic. This IAS postdoctoral grant is focused upon these two broad research questions, as it has allowed me to conduct fieldwork near Hornsundneset (Fig. 1) in August 2022, as well as running a thorough provenance analysis of the Brevassfjellet conglomerate beds (Fig. 5). This field campaign was also made possible thanks to the CASP Andrew Whitham Fieldwork Awards.

2. Methods

Fieldwork was conducted in Summer 2022 in the Festningen, Reinodden, and Hornsundneset areas, during which six sections were measured (Fig. 1-2-3). Standard techniques in lithofacies analysis and architectural–element analysis have been used in order to interpret depositional processes and the depositional settings of these sedimentary rocks. The types and degree of bioturbation were documented for all measured sections by members of the project team.

Logging of these sedimentary sections in Hornsundneset was accompanied by targeted sampling of specific beds: the bentonite tephra bed at the base of the conglomerate unit on Sergeevfjellet was sampled (ca. 2 kg) for U-Pb dating of volcanic zircons (Fig. 3-4), which will constrain the onset of sedimentation on the SHH. Eight conglomerate samples (ca. 20 kg) were collected to conduct thin section and XRD analyses on these deposits. The thin-section analysis was conducted on an Olympus BH-2 microscope using both plane- and cross-polarised light (Fig. 3-4). A D2 Phaser by Bruker with an SSD160-2 Detector, based at the Geological Institute of RWTH-Aachen University, was used for X-ray diffraction analyses. Mineral-phase identification was conducted with the DIFFRAC.EVA software and the quantitative analysis with DIFFRAC.TOPAS. Two representative conglomerate samples from the Sergeevfjellet and Lidfjellet sections (Fig. 1-3) have been used for provenance analysis (yielding 262 individual age analysis). The provenance analysis was conducted at the UTChron Laboratories (Thermochronology Lab) at the Jackson School of Geoscience at the University of Texas at Austin, USA. For the analysis we used Laser Ablation Inductively Coupled Plasma Mass Spectrometry (LA-ICP-MS). In addition, two intra-conglomerate, fossil-rich, carbonate beds were sampled (ca. 10 kg) for biostratigraphy analyses. The dating of the tephra bed as well as the biostratigraphy analysis are still ongoing by members of the project team.

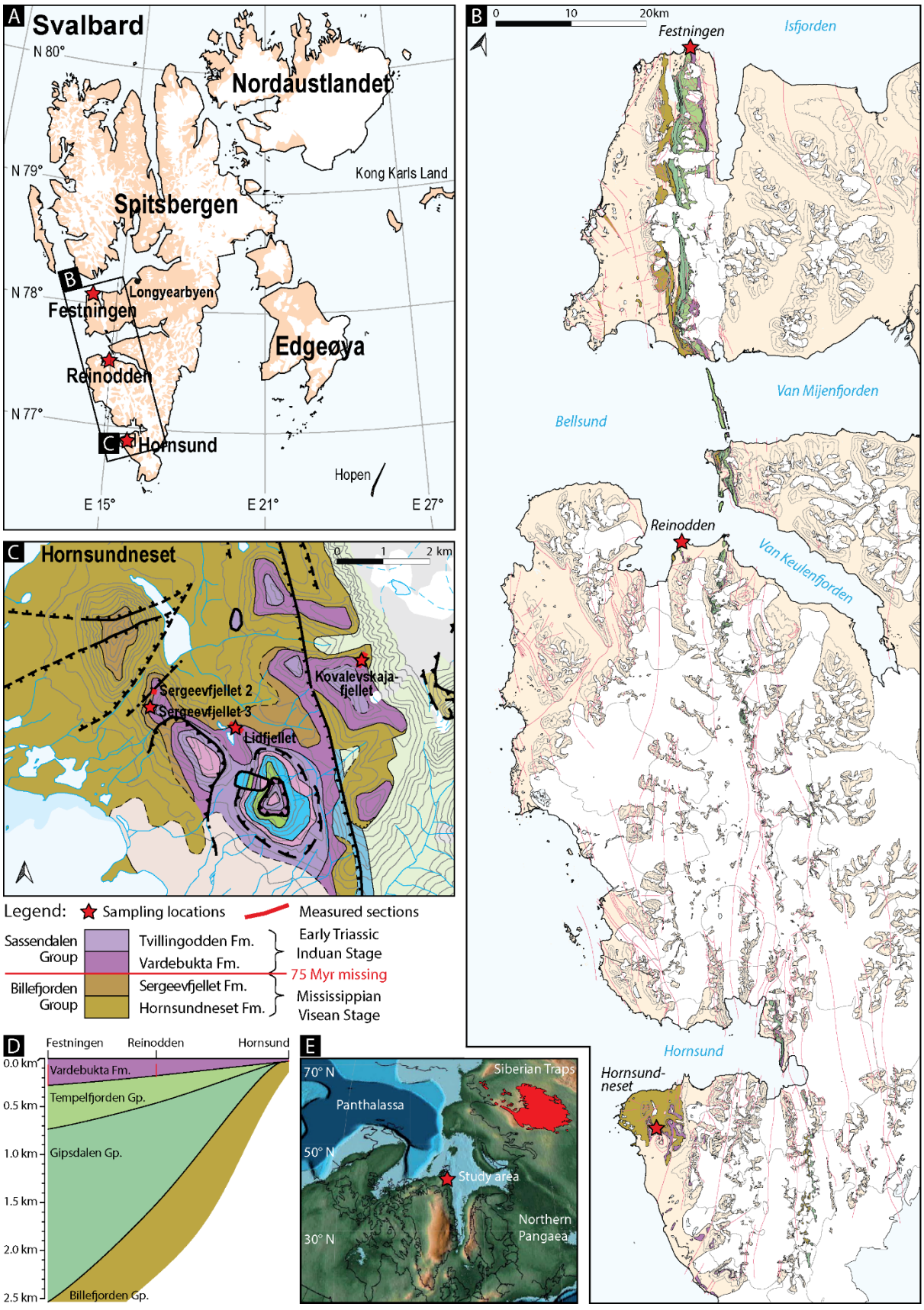

Fig. 1 – A. Overview map of Svalbard. B. Modified geological map of western Spitsbergen highlighting the targeted Carboniferous to Lower Triassic units as well as the three visited localities of Festningen, Reinodden, and Hornsundneset. C. Geological map of the Hornsundneset area, displaying the location of the four measured sections (maps from the Norwegian Polar Institute). D. Schematic cross-section showing the thickness variations between the different localities. E. Palaeogeographical map at the end of the Permian, ca. 252 Ma (modified from the Scotese Paleomap Project).

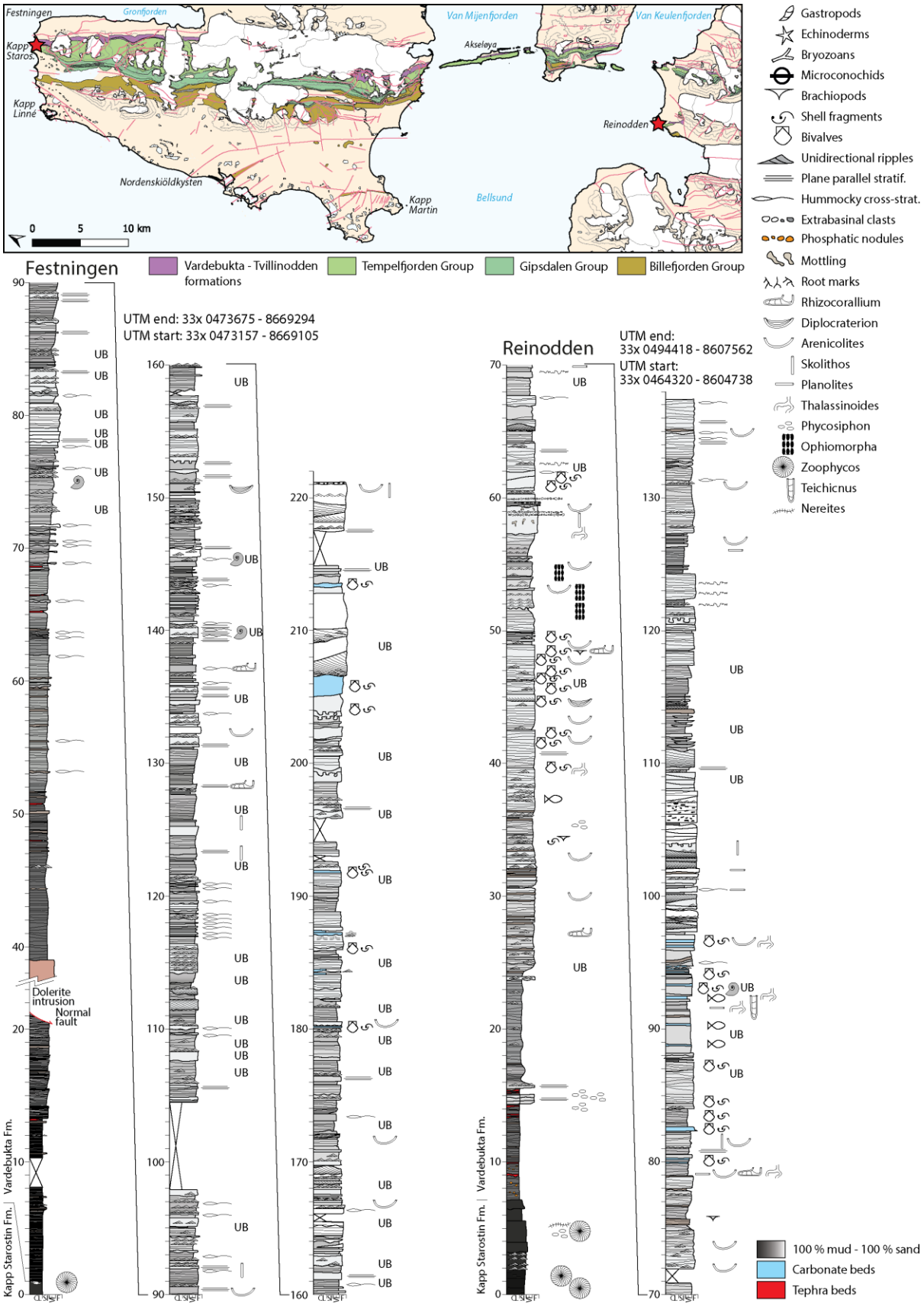

Fig. 2 – Sedimentological logs of the Festningen and Reinodden sections with zoomed-in geological map of western Spitsbergen (map adapted from the Norwegian Polar Institute).

3. Results and conclusions:

To the north of the SHH, a siliciclastic-dominated shelfal system developed following the supra-regional transgression occurring very rapidly at the very end of the Permian, as recorded at the top of the Kapp Starostin Formation and exposed at the Reinodden and Festningen sections (Fig. 2; Mørk et al., 1989). Multiple upward-coarsening and upward-fining intervals were recognised in these shelfal successions, both of which are characterised by an overall upward-coarsening trend. Fossiliferous limestone beds occur in both Reinodden and Festningen, testifying of local temporary reduction in siliciclastic sediment supply. Overall, the sedimentary succession at Reinodden is thinner but sandier than in Festningen, and these sandier intervals are also thicker at Reinodden. *Zoophycos* trace fossils can be observed near the base of both sections, whereas *Skolithos*, *Arenicolites*, and *Diplocriterion* occur in sandier intervals up-section (Fig. 2). These observations confirm that the sedimentary succession at Reinodden was deposited closer to the SHH in an environment subject to lower rates of accommodation creation and sediment accumulation in comparison to the more distal Festningen section. The documented upward-coarsening and upward-fining facies patterns are likely indicative of shallowing and deepening water-depth trends, respectively, with the coarser strata deposited under higher depositional energy. The nature of the observed trends, however, remain to be further investigated, as along-strike autogenic variations as well as allogenic forcings (or a combination of both) could generate such cyclical patterns.

Dating of the tephra bed at the base of the Brevassfjellet Beds on the SHH is ongoing. However, the currently available data indicate that the volcanic sediments show similar characteristics to the lowermost bentonite beds outcropping in western and central Spitsbergen. These include similar colouration of weathered and unweathered strata, sedimentary texture, thickness, and unconsolidated nature (Fig. 4; Zuchuat et al., 2020). This tephra layer is overlain by a polymictic, matrix- to clast-supported conglomerate and gravelly-sandstone interval, which varies in thickness from 2 to 7 m between Kovalevskajafjellet and Sergeevfjellet and shows high lateral variation in composition and stacking architecture (Fig. 3-4). While detrital mono- and polycrystalline quartz grains are the main constituent in most Brevassfjellet conglomeratic beds, the amount and type of cement varies significantly, with ankerite (Fe-, Mn-, Mg-rich carbonate), dolomite, and calcite varying between a few % to up to 77 % in sample SF_6.40 (Fig. 3). The occurrence of well-defined, 20 cm deep rhizoliths in some of these conglomeratic beds, as visible on Sergeevfjellet (Fig. 3–4), are indicative of vegetation growth at the surface of these sediments. Evidence for limited but periodic vegetation cover associated with the limited thickness of this conglomeratic interval and the presence of ankerite and dolomite suggest a low sedimentation-rate and low accommodation-rate arid- to semi-arid continental system. Data indicate that mass-flows and ephemeral streams periodically occurred in some places, whereas other parts of the system were sediment-starved. These continental deposits are capped by fossiliferous marine limestone containing gastropod fragments, brachiopod- and bivalve-shell fragments, echinoderm fragments, microconochids, Dienerian bryozoan fragments (Zuchuat, 2014) and pore-filling calcite spar (Fig. 3). Gastropod shells sometimes display geopetal infill. These fossiliferous limestone beds thicken and increase in number eastwards towards the palaeoshoreline, reaching a maximum thickness of 40 cm per bed at Kovalevskajafjellet, while only one, ca. 10 cm-thick bed occurs on Sergeevfjellet (Fig. 4). Furthermore, these fossiliferous limestone beds are characterised by a decrease in siliciclastic content associated with an increase in diversity and number of preserved fossil fragments towards the palaeoshoreline (Fig. 3-4). These characteristics indicate deposition in a well-oxygenated shallow-marine environment, in which the current energy was sufficiently high to wash away any potential micrite or mud, allowing for the precipitation of sparry calcite instead. These limestone beds are overlain by a coarsening-upward, mud-rich interval in which individual very-fine to fine sandstone beds occur; the thickness and frequency of these sandstone beds also increase up-section (Fig. 4).

These sandstone beds are sharp-based with no normal or reverse grading and can be either structureless or display hummocky cross-stratification (HCS), combined-flow ripples, (occasionally climbing) unidirectional current ripples, slight undulation, or plane-parallel stratification (Fig. 3-4).

The provenance analysis of the two tested conglomeratic samples SF_8.85 and Lid_0.9 shows a polymodal distribution of detrital zircon ages, with major Palaeozoic, Mesoproterozoic–Palaeoproterozoic as well as the Archean age modes (Fig. 5). These two samples show similar cumulative-distribution patterns as the detrital zircons from the Vardebukta Formation at Festningen (Gilmullina et al., 2023). These two samples also show very strong affinities to the zircon ages reported by Bjerager et al. (2023) from the Induan-aged Parish Bjerg Formation deposited on northern Laurentia and cropping out today in Greenland.

In summary, data collected for this project indicate that preservation of deposited sediment on the SHH resumed shortly after the onset of the eruption phase of the Siberian Traps Large Igneous Province, ending a hiatus that lasted more than 75 Myr with the deposition of a thick bentonite tephra bed. This tephra layer is overlain by polymictic, conglomerate-rich alluvial fans and potentially braided-river deposits on which superficial and ephemeral vegetation developed. Short-lived episodes of relative sea-level rise led to the intermittent deposition of fossiliferous, shallow-marine calcareous beds onto the fringe of the alluvial fans sourced from Greenlandic terranes before a final major transgression of the whole continental domain in the Dienerian and the onset of siliciclastic-dominated shelfal sedimentation over the area. This major transgression was followed by an overall shallowing-upward trend recorded by regular event beds, reflecting episodic hyperpycnal-like events or events combining unidirectional and oscillatory currents, potentially (Jelby et al., 2020) though not necessarily (Wu et al., 2024) associated with storms.

This Dienerian flooding of the SHH followed by shelfal deposits of the Vardebukta Formation, however, contrasts with the basin dynamics recorded by the Vardebukta Formation away from the High, which recorded an overall transgression and regression potentially punctuated by shorter-lasting transgression-regression episodes. None of these shorter-lasting transgression-regression episodes seem to correlate with the Dienerian transgression that flooded the High. This apparent dichotomy suggests that the flooding of the SHH could be explained by local tectonic subsidence rather than eustatic sea-level rise.

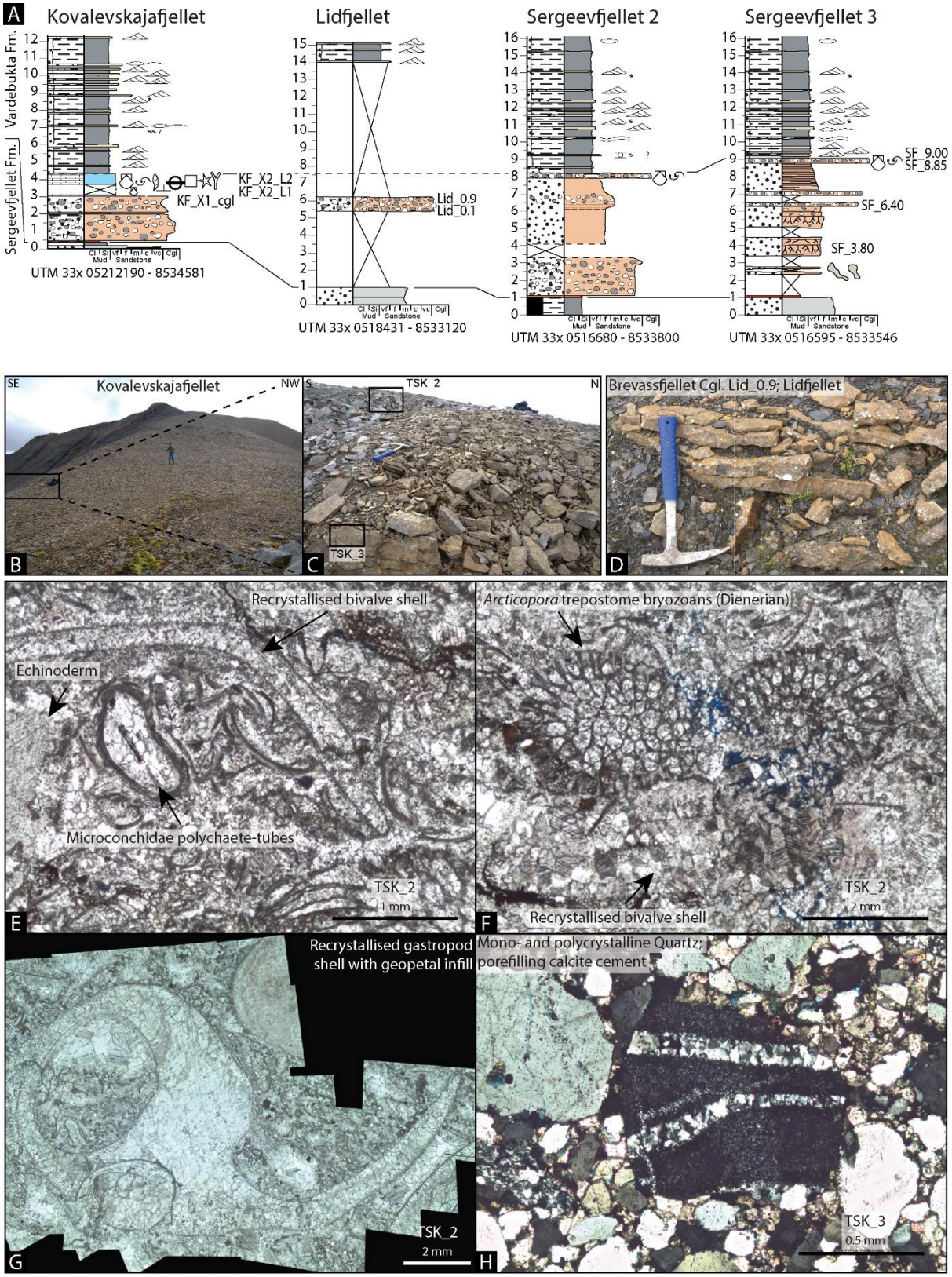

Fig. 3 – A. Sedimentary logs of the measured section on Hornsundneset. See Fig. 1 for location, Fig. 2 for legend. B-C. Outcrop photo of Kovalevskajafjellet with indication of where samples represented by thin-sections TSK_2 and TSK_3. D were collected. Outcrop photo illustrating the only exposed bed of the Brevassfjellet conglomerate near Lidfjellet. E-F-G-H. Microphotographs of thin sections TSK_2 and TSK_3 from Kovalevskajafjellet.

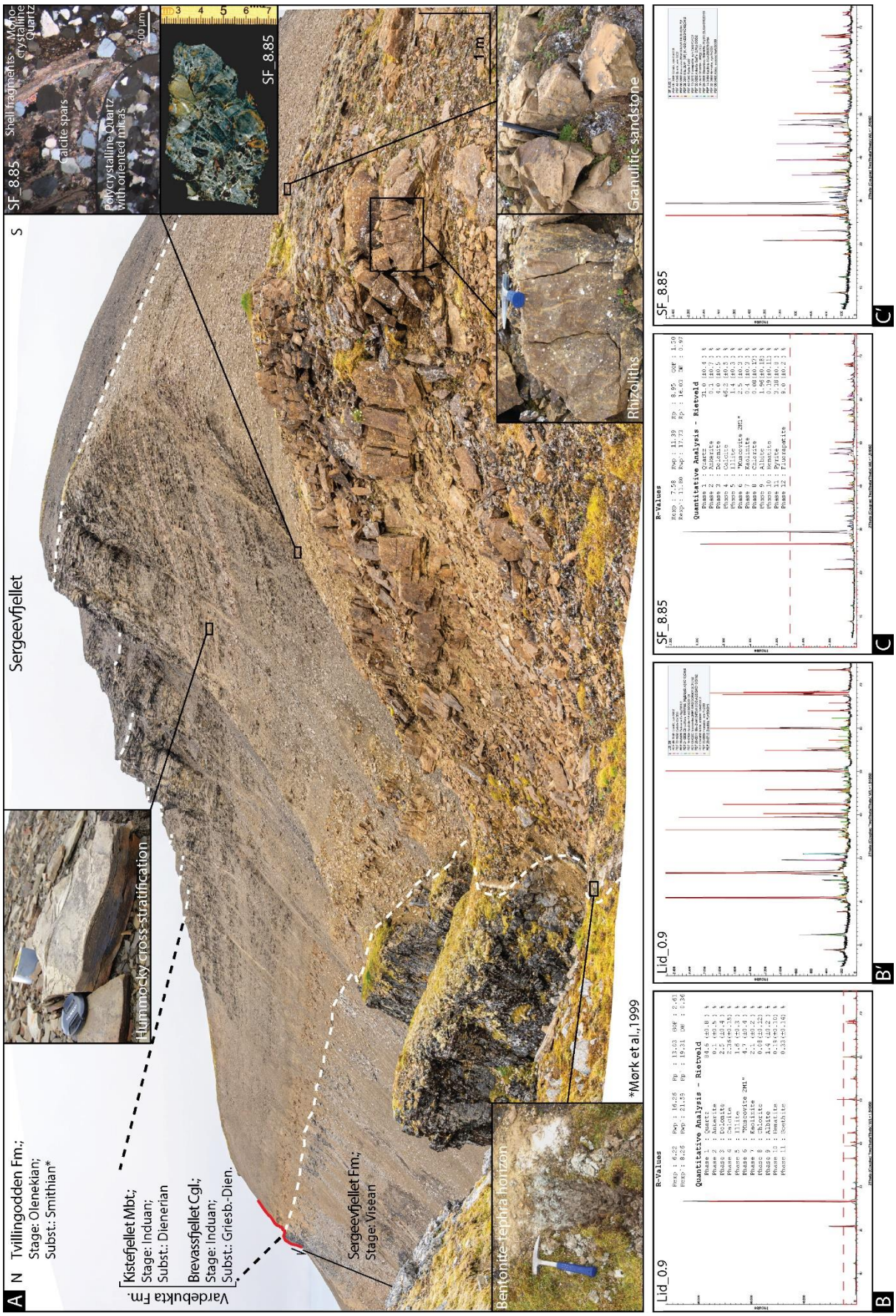

Fig. 4 – A. Outcrop photo at Sergeevfjellet showing the Carboniferous Sergeevfjellet Formation, overlain by the bentonite tephra bed at the base of the Brevasfjellet conglomerate, with some of the beds showing well-developed rhizoliths. Inset photos also show the topmost fossiliferous, clast-rich bed at the top of the Brevassfjellet conglomerate before the major Dienerian flooding associated with the

development of more shelfal deposition punctuated with event beds, some of which show clear hummocky cross-stratification. B-B'. XRD results of the LID_0.9 sample from the Lidfjellet section. The black line is the bulk signal from the sample, the other colours on the spectrum are the different mineral phases. The red dashed-box in B indicates the position of the zoomed-in B'-view. C-C'. XRD results of the SF_8.85 sample from Sergeevfjellet section. The black line is the bulk signal from the sample, the other colours on the spectrum are the different mineral phases. The red dashed-box in C indicates the position of the zoomed-in C'-view. Detailed XRD results in appendices.

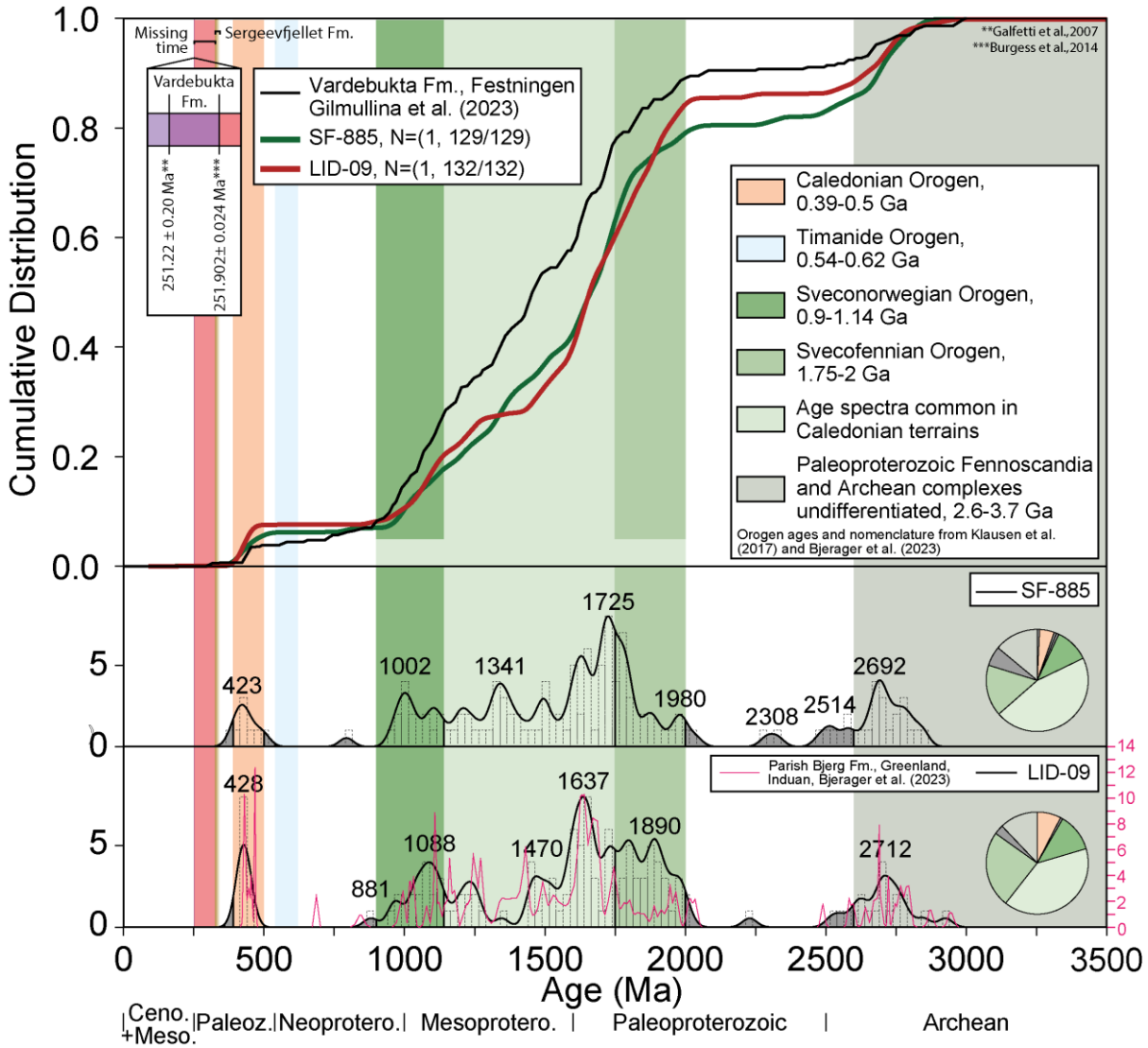

Fig. 5 – Top: Cumulative distribution of zircon ages from the two analysed samples SF_8.85 (green line) and LID_0.9 (red line; this study), compared with the data from the Vardebukta Formation at Festningen (from Gilmullina et al., 2023), with the different major tectonic events after Klausen et al. (2017) and Bjerager et al. (2023). The diagram also highlights the time representing the Sergeevfjellet Formation (dark brown vertical band), the duration of the 75 Myr hiatus (vertical red band), and the very short time representing the deposition of the Vardebukta Formation (purple band in the inset box). Bottom: zircon-age distribution of the two samples, SF_8.85 and LID_0.9. The pink line plots the zircon age distribution of the Induan-aged Parish Bjerg Formation from Greenland (Bjerager et al., 2023).

References:

Bjerager, M., Alsen, P., Bojesen-Koefoed, J. A., Fyhn, M. B., Hovikoski, J., Keulen, N., ... & Thomsen, T. B. (2023). Triassic in the northernmost Atlantic—Linking North Greenland and the southwestern Barents Sea. *Terra Nova*, *35*(4), 250-259.

Burgess, S. D., Bowring, S., & Shen, S. Z. (2014). High-precision timeline for Earth's most severe extinction. *Proceedings of the National Academy of Sciences*, *111*(9), 3316-3321.

Cutbill, J.L., Challinor, A. (1965). Revision of the stratigraphical scheme for the Carboniferous and Permian rocks of Spitsbergen and Bjørnøya. *Geol. Mag. 102 (5)*, 418–439.

Dallmann, W.K (1999). Introduction. In: Dallmann, W.K. (Ed.), *Lithostratigraphic Lexicon of Svalbard*. Norsk Polarinstitutt, Tromsø, 11-24.

Galfetti, T., Hochuli, P. A., Brayard, A., Bucher, H., Weissert, H., & Vigran, J. O. (2007). Smithian-Spathian boundary event: Evidence for global climatic change in the wake of the end-Permian biotic crisis. *Geology*, *35*(4), 291-294.

Gilmullina, A., Klausen, T. G., Paterson, N. W., Suslova, A., & Eide, C. H. (2021). Regional correlation and seismic stratigraphy of Triassic Strata in the Greater Barents Sea: Implications for sediment transport in Arctic basins. *Basin research*, *33*(2), 1546-1579.

Gilmullina, A., Klausen, T. G., Doré, A. G., Sirevaag, H., Suslova, A., & Eide, C. H. (2023). Arctic sediment routing during the Triassic: sinking the Arctic Atlantis. *Journal of the Geological Society*, *180*(1), jgs2022-018.

Jelby, M. E., Grundvåg, S. A., Helland-Hansen, W., Olaussen, S., & Stemmerik, L. (2020). Tempestite facies variability and storm-depositional processes across a wide ramp: Towards a polygenetic model for hummocky cross-stratification. *Sedimentology*, *67*(2), 742-781.

Klausen, T. G., Müller, R., Slama, J., & Helland-Hansen, W. (2017). Evidence for Late Triassic provenance areas and Early Jurassic sediment supply turnover in the Barents Sea Basin of northern Pangea. *Lithosphere*, *9*(1), 14-28.

Mørk, A., Knarud, R., Worsley, D. (1982). Depositional and diagnetic environments of the Triassic and lower Jurassic succession of Svalbard. In: Embry, A.F., Balkwill, H.R. (Eds.), *Arctic Geology and Geophysics*, Canadian Society of Petroleum Geologist, Calgary, Alberta, Canada, Memoir. 8. 371-398.

Mørk, A., Embry, A., Weitschat, W., 1989. Triassic transgressive-regressive cycles in the Sverdrup basin, Svalbard and Barents shelf. In: Collinson, J.D. (Ed.), *Correlation in Hydrocarbon Exploration*, Proceedings of a Norwegian Society Conference, Graham and Trotman, London, pp. 113-130.

Mørk, A., Elvebakk, G., Forsberg, A.W., Hounslow, M.W., Nakrem, H.A., Vigran, J.O., Weitschat, W. (1999a). The type section of the Vikinghogda Formation: a new Lower Triassic unit in central and eastern Svalbard. *Polar Res. 18 (1)*, 51-82.

Mørk, A., Dallmann, W.K., Dypvik, H., Johannessen, E.P., Larsen, G.B., Nagy, J., Nøttvedt, A., Olaussen, S., Pcelina, T.M., Worsley, D. (1999b). Mesozoic lithostratigraphy. In: Dallmann (Ed.), *Lithostratigraphic Lexicon of Svalbard*. Norsk Polarinstitutt, Tromsø, pp. 127-214.

Smyrak-Sikora, A., Augland, L.E., Betlem, P., Engelschiøn, V.S., Faleide, J.I., Foster, W.J., Galloway, J.M., Grundvåg, S.-A., Jelby, M.E., Jensen, M.A., Jochmann, M.M., Johannessen, E.P., Jones, M.T., Koevoets, M., Kulhanek, D., Lord, G.S., Mosociova, T., Mørk, A., Olaussen, S., Planke, S., Price, G.D., Senger, K., Shephard, G.E., Śliwińska, K.K., Stemmerik, L., Vickers, M.L., & Zuchuat, V. (in review). Phanerozoic paleoenvironmental and paleoclimatic evolution in Svalbard, Norway. Submitted to *Climate of the past*.

Svensen, H., Planke, S., Polozov, A. G., Schmidbauer, N., Corfu, F., Podladchikov, Y. Y., & Jamtveit, B. (2009). Siberian gas venting and the end-Permian environmental crisis. *Earth and Planetary Science Letters*, *277*(3-4), 490-500.

Wu, X., Carling, P. A., & Parsons, D. (2024). Hummocky sedimentary structures within rippled beds due to combined orbital waves and transverse currents. *Sedimentology*, *71*(2), 573-589.

Zuchuat, V. (2014). A Sedimentary Investigation of the Lower Triassic Formations and Their Underlying Permo-Carboniferous Units Across Spitsbergen, Svalbard. Master's thesis. Department of Geology and Mineral Resources Engineering, Norwegian University of Science and Technology, Norway (2014), 1-167.

Zuchuat, V., Sleveland, A. R. N., Twitchett, R. J., Svensen, H. H., Turner, H., Augland, L. E., ... & Planke, S. (2020). A new high-resolution stratigraphic and palaeoenvironmental record spanning the End-Permian Mass Extinction and its aftermath in central Spitsbergen, Svalbard. *Palaeogeography, Palaeoclimatology, Palaeoecology*, *554*, 109732.

Appendices

KF_X1_CGL

Hauptkomponenten: Quarz, Ankerit/Dolomit, Calcit
Nebenkomponenten: Tonminerale/Glimmer, Chlorit, Goethit; evtl. Feldspat
Zoom: Hauptkomponenten: Quarz, Ankerit/Dolomit, Calcit
Nebenkomponenten: Tonminerale/Glimmer, Chlorit, Goethit; evtl. Feldspat

Range Number : 1

R-Values

Rexp : 7.01 Rwp : 11.69 Rp : 9.13 GOF : 1.67
Rexp`: 11.03 Rwp`: 18.38 Rp` : 16.69 DW : 0.76

Quantitative Analysis - Rietveld

Phase 1 : Quartz	28.8 (±0.3) %
Phase 2 : Ankerite	13.6 (±0.5) %
Phase 3 : Dolomite	37.8 (±0.6) %
Phase 4 : Calcite	10.22(±0.19) %
Phase 5 : Illite	0.99(±0.17) %
Phase 6 : "Muscovite 2M1"	4.2 (±0.4) %
Phase 7 : Kaolinite	0.53(±0.12) %
Phase 8 : Chlorite	1.8 (±0.2) %
Phase 9 : Albite	0.33(±0.16) %
Phase 10 : Goethite	1.69(±0.12) %

KF_X2_L1

Hauptkomponenten: Calcit, Quarz
Nebenkomponenten: Ankerit/Dolomit, Tonminerale/Glimmer, Chlorit, Feldspat, Pyrit; evtl. Hämatit
Zoom: Hauptkomponenten: Calcit, Quarz
Nebenkomponenten: Ankerit/Dolomit, Tonminerale/Glimmer, Chlorit, Feldspat, Pyrit; evtl. Hämatit

Range Number : 1

R-Values

Rexp : 7.71 Rwp : 13.83 Rp : 10.99 GOF : 1.79
Rexp`: 10.97 Rwp`: 19.66 Rp` : 17.82 DW : 0.67

Quantitative Analysis - Rietveld

Phase 1 : Quartz	18.3(±0.2) %
Phase 2 : Ankerite	0.0(±0.7) %
Phase 3 : Dolomite	2.1(±0.4) %
Phase 4 : Calcite	70.8(±0.7) %
Phase 5 : Illite	0.9(±0.2) %
Phase 6 : "Muscovite 2M1"	3.3(±0.3) %
Phase 7 : Kaolinite	0.4(±0.4) %
Phase 8 : Chlorite	0.09(±0.18) %
Phase 9 : Albite	3.41(±0.17) %
Phase 10 : Hematite	0.20(±0.10) %
Phase 11 : Pyrite	0.53(±0.7) %

KF_X3_L2
Hauptkomponenten: Calcit
Nebenkomponenten: Quarz, Tonminerale/Glimmer, Chlorit, Feldspat, Hämatit, Goethit, Pyrit; evtl.: Markasit, Ankerit, Dolomit
Zoom: Hauptkomponenten: Calcit
Nebenkomponenten: Quarz, Tonminerale/Glimmer, Chlorit, Feldspat, Hämatit, Goethit, Pyrit; evtl.: Markasit, Ankerit, Dolomit

Range Number : 1

R-Values
Rexp : 7.70 Rwp : 15.91 Rp : 12.50 GOF : 2.07
Rexp`: 10.53 Rwp`: 21.78 Rp` : 19.69 DW : 0.53

Quantitative Analysis - Rietveld

Phase 1 : Quartz	7.61(±0.15) %
Phase 2 : Ankerite	0.0 (±0.6) %
Phase 3 : Dolomite	0.3 (±0.2) %
Phase 4 : Calcite	87.4 (±0.8) %
Phase 5 : Illite	0.8 (±0.2) %
Phase 6 : "Muscovite 2M1"	1.9 (±0.3) %
Phase 7 : Kaolinite	0.1 (±0.4) %
Phase 8 : Chlorite	0.08(±0.15) %
Phase 9 : Albite	0.47(±0.11) %
Phase 10 : Hematite	0.00(±0.4) %
Phase 11 : Pyrite	0.57(±0.11) %
Phase 12 : Marcasite	0.62(±0.14) %
Phase 13 : Goethite	0.05(±0.6) %

LID_01_oben
Hauptkomponenten: Quarz
Nebenkomponenten: Ankerit/Dolomit, Calcit, Tonminerale/Glimmer, Chlorit, Feldspat, Pyrit, Hämatit; evtl. Fluorapatit
Zoom: Hauptkomponenten: Quarz
Nebenkomponenten: Ankerit/Dolomit, Calcit, Tonminerale/Glimmer, Chlorit, Feldspat, Pyrit, Hämatit; evtl. Fluorapatit

Range Number : 1

R-Values

Rexp : 6.48 Rwp : 12.72 Rp : 9.80 GOF : 1.96
Rexp`: 8.68 Rwp`: 17.03 Rp` : 14.36 DW : 0.60

Quantitative Analysis - Rietveld

Phase 1 : Quartz	68.6 (±0.5) %
Phase 2 : Ankerite	0.3 (±0.3) %
Phase 3 : Dolomite	11.2 (±0.3) %
Phase 4 : Calcite	1.42(±0.13) %
Phase 5 : Illite	3.0 (±0.2) %
Phase 6 : "Muscovite 2M1"	10.0 (±0.4) %
Phase 7 : Kaolinite	3.20(±0.17) %
Phase 8 : Chlorite	0.08(±0.9) %
Phase 9 : Albite	1.46(±0.17) %
Phase 10 : Hematite	0.22(±0.7) %
Phase 11 : Pyrite	0.20(±0.6) %
Phase 12 : Fluorapatite	0.28(±0.13) %

LID_01_unten
Hauptkomponenten: Quarz
Nebenkomponenten: Dolomit, Tonminerale/Glimmer, Chlorit/Kaolinit, Calcit, Feldspat, Markasit, Hämatit; evtl. Fluorapatit
Zoom: Hauptkomponenten:Quarz
Nebenkomponenten: Dolomit, Tonminerale/Glimmer, Chlorit/Kaolinit, Calcit, Feldspat, Markasit, Hämatit; evtl. Fluorapatit

Range Number : 1

R-Values

Rexp : 6.43 Rwp : 14.05 Rp : 11.22 GOF : 2.18
Rexp`: 8.59 Rwp`: 18.75 Rp` : 16.44 DW : 0.49

Quantitative Analysis - Rietveld

Phase 1 : Quartz	73.0 (±0.6) %
Phase 2 : Ankerite	0.2 (±0.3) %
Phase 3 : Dolomite	7.3 (±0.4) %
Phase 4 : Calcite	0.76(±0.14) %
Phase 5 : Illite	4.0 (±0.3) %
Phase 6 : "Muscovite 2M1"	10.4 (±0.4) %
Phase 7 : Kaolinite	2.70(±0.18) %
Phase 8 : Chlorite	0.0 (±0.2) %
Phase 9 : Albite	1.05(±0.19) %
Phase 10 : Hematite	0.10(±0.06) %
Phase 11 : Marcasite	0.38(±0.9) %
Phase 12 : Fluorapatite	0.11(±0.6) %

LID_09
Hauptkomponenten: Quarz
Nebenkomponenten: Calcit, Dolomit, Chlorit/Kaolinit, Tonminerale/Glimmer, Feldspat; evtl.: Hämatit, Goethit
Zoom: Hauptkomponenten: Quarz
Nebenkomponenten: Calcit, Dolomit, Chlorit/Kaolinit, Tonminerale/Glimmer, Feldspat; evtl.: Hämatit, Goethit

Range Number : 1

R-Values

Rexp : 6.22 Rwp : 16.26 Rp : 13.03 GOF : 2.61
Rexp`: 8.26 Rwp`: 21.59 Rp` : 19.31 DW : 0.36

Quantitative Analysis - Rietveld

Phase 1 : Quartz	84.6 (±0.8) %
Phase 2 : Ankerite	0.1 (±0.5) %
Phase 3 : Dolomite	2.5 (±0.4) %
Phase 4 : Calcite	2.36(±0.15) %
Phase 5 : Illite	1.6 (±0.3) %
Phase 6 : "Muscovite 2M1"	4.7 (±0.4) %
Phase 7 : Kaolinite	2.1 (±0.2) %
Phase 8 : Chlorite	0.08(±0.12) %
Phase 9 : Albite	1.4 (±0.2) %
Phase 10 : Hematite	0.19(±0.10) %
Phase 11 : Goethite	0.33(±0.14) %

SF_3.80
Hauptkomponenten: Quarz, Dolomit/Ankerit
Nebenkomponenten: Tonminerale/Glimmer, Chlorit/Kaolinit, Calcit, Feldspat, Fluorapatit; evtl.: Pyrit
Zoom: Hauptkomponenten: Quarz, Dolomit/Ankerit
Nebenkomponenten: Tonminerale/Glimmer, Chlorit/Kaolinit, Calcit, Feldspat, Fluorapatit; evtl.: Pyrit

Range Number : 1

R-Values

Rexp : 6.72 Rwp : 12.31 Rp : 9.47 GOF : 1.83
Rexp`: 9.97 Rwp`: 18.28 Rp` : 15.91 DW : 0.66

Quantitative Analysis - Rietveld

Phase 1 : Quartz	51.4 (±0.5) %
Phase 2 : Ankerite	10.5 (±0.4) %
Phase 3 : Dolomite	19.9 (±0.5) %
Phase 4 : Calcite	0.75(±0.14) %
Phase 5 : Illite	4.3 (±0.3) %
Phase 6 : "Muscovite 2M1"	4.7 (±0.3) %
Phase 7 : Kaolinite	3.0 (±0.2) %
Phase 8 : Chlorite	0.07(±0.14) %
Phase 9 : Albite	2.27(±0.19) %
Phase 10 : Pyrite	0.43(±0.7) %
Phase 11 : Fluorapatite	2.62(±0.15) %

SF_6.40
Hauptkomponenten: Dolomit/Ankerit, Quarz
Nebenkomponenten: Tonminerale/Glimmer, Chlorit/Kaolinit, Calcit, Feldspat, Pyrit, Fluorapatit; evtl.: Hämatit
Zoom: Hauptkomponenten: Dolomit/Ankerit, Quarz
Nebenkomponenten: Tonminerale/Glimmer, Chlorit/Kaolinit, Calcit, Feldspat, Pyrit, Fluorapatit; evtl.: Hämatit

Range Number : 1

R-Values

Rexp : 7.33 Rwp : 13.08 Rp : 10.15 GOF : 1.78
Rexp`: 11.30 Rwp`: 20.16 Rp` : 18.12 DW : 0.66

Quantitative Analysis - Rietveld

Phase 1 : Quartz	10.73(±0.13) %
Phase 2 : Ankerite	2.8 (±0.2) %
Phase 3 : Dolomite	77.9 (±0.5) %
Phase 4 : Calcite	0.48(±0.15) %
Phase 5 : Illite	2.0 (±0.2) %
Phase 6 : "Muscovite 2M1"	2.2 (±0.2) %
Phase 7 : Kaolinite	0.76(±0.15) %
Phase 8 : Chlorite	0.23(±0.11) %
Phase 9 : Albite	0.43(±0.18) %
Phase 10 : Hematite	0.65(±0.11) %
Phase 11 : Pyrite	0.39(±0.7) %
Phase 12 : Fluorapatite	1.4 (±0.2) %

SF_8.85_1
Hauptkomponenten: Calcit, Quarz
Nebenkomponenten: Tonminerale/Glimmer, Pyrit, Fluorapatit, Dolomit/Ankerit, Chlorit/Kaolinit, Feldspat, Hämatit
Zoom: Hauptkomponenten: Calcit, Quarz
Nebenkomponenten: Tonminerale/Glimmer, Pyrit, Fluorapatit, Dolomit/Ankerit, Chlorit/Kaolinit, Feldspat, Hämatit

Range Number : 1

R-Values

Rexp : 7.58 Rwp : 11.39 Rp : 8.95 GOF : 1.50
Rexp`: 11.80 Rwp`: 17.73 Rp` : 16.03 DW : 0.97

Quantitative Analysis - Rietveld

Phase 1 : Quartz	31.0 (±0.4) %
Phase 2 : Ankerite	0.1 (±0.7) %
Phase 3 : Dolomite	4.0 (±0.5) %
Phase 4 : Calcite	46.2 (±0.5) %
Phase 5 : Illite	1.4 (±0.3) %
Phase 6 : "Muscovite 2M1"	2.5 (±0.3) %
Phase 7 : Kaolinite	0.4 (±0.3) %
Phase 8 : Chlorite	0.08(±0.17) %
Phase 9 : Albite	1.96(±0.18) %
Phase 10 : Hematite	0.19(±0.11) %
Phase 11 : Pyrite	3.18(±0.8) %
Phase 12 : Fluorapatite	9.0 (±0.2) %

SF_9.00
Hauptkomponenten: Quarz, Calcit
Nebenkomponenten: Fluorapatit, Pyrit, Tonminerale/Glimmer, Dolomit/Ankerit, Chlorit/Kaolinit; evtl.: Hämatit, Feldspat
Zoom: Hauptkomponenten: Quarz, Calcit
Nebenkomponenten: Fluorapatit, Pyrit, Tonminerale/Glimmer, Dolomit/Ankerit, Chlorit/Kaolinit; evtl.: Hämatit, Feldspat

Range Number : 1

R-Values

Rexp : 6.77 Rwp : 11.73 Rp : 9.23 GOF : 1.73
Rexp`: 11.28 Rwp`: 19.56 Rp` : 18.55 DW : 0.71

Quantitative Analysis - Rietveld

Phase 1 : Quartz	55.8 (±0.6) %
Phase 2 : Ankerite	0.0 (±0.6) %
Phase 3 : Dolomite	0.5 (±0.3) %
Phase 4 : Calcite	18.9 (±0.3) %
Phase 5 : Illite	2.0 (±0.4) %
Phase 6 : "Muscovite 2M1"	1.5 (±0.5) %
Phase 7 : Kaolinite	0.98(±0.19) %
Phase 8 : Chlorite	0.66(±0.12) %
Phase 9 : Albite	1.6 (±0.2) %
Phase 10 : Hematite	0.44(±0.13) %
Phase 11 : Pyrite	1.89(±0.9) %
Phase 12 : Fluorapatite	15.6 (±0.3) %

SF_NG_8.00
Hauptkomponenten: Quarz, Calcit
Nebenkomponenten: Tonminerale/Glimmer, Feldspat, Chlorit/Kaolinit, Fluorapatit, Pyrit, Dolomit/Ankerit, evtl.: Hämatit
Zoom: Hauptkomponenten: Quarz, Calcit
Nebenkomponenten: Tonminerale/Glimmer, Feldspat, Chlorit/Kaolinit, Fluorapatit, Pyrit, Dolomit/Ankerit, evtl.: Hämatit

Range Number : 1

R-Values

Rexp : 7.13 Rwp : 14.33 Rp : 11.28 GOF : 2.01
Rexp`: 10.36 Rwp`: 20.83 Rp` : 18.74 DW : 0.56

Quantitative Analysis - Rietveld

Phase 1 : Quartz	48.2 (±0.4) %
Phase 2 : Ankerite	0.1 (±0.3) %
Phase 3 : Dolomite	0.5 (±0.2) %
Phase 4 : Calcite	38.0 (±0.3) %
Phase 5 : Illite	1.6 (±0.2) %
Phase 6 : "Muscovite 2M1"	7.2 (±0.4) %
Phase 7 : Kaolinite	0.4 (±0.2) %
Phase 8 : Chlorite	0.30(±0.11) %
Phase 9 : Albite	2.5 (±0.2) %
Phase 10 : Hematite	0.56(±0.11) %
Phase 11 : Pyrite	0.64(±0.9) %